# Thermal and statistical analysis of the high-Z tungsten-based UFOs observed during the first deuterium high fluence campaign of the WEST tokamak

J. Gaspar, Y. Anquetin, Y. Corre, X. Courtois, M. Diez, A. Ekedahl, N. Fedorczak, A. Gallo, J-L. Gardarein, J. Gerardin, et al.

Nuclear Materials and Energy 41 (2024) 101745

Contents lists available at ScienceDirect

Nuclear Materials and Energy

journal homepage: www.elsevier.com/locate/nme

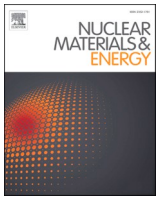

# Thermal and statistical analysis of the high-Z tungsten-based UFOs observed during the first deuterium high fluence campaign of the WEST tokamak

J. Gaspar [a,*], Y. Anquetin [a], Y. Corre [b], X. Courtois [b], M. Diez [b], A. Ekedahl [b], N. Fedorczak [b], A. Gallo [b], J-L. Gardarein [a], J. Gerardin [b], J. Gunn [b], A. Grosjean [c], K. Krieger [d], T. Loarer [b], P. Manas [b], C. Martin [e], P. Maget [b], R. Mitteau [b], P. Moreau [b], F. Rigollet [a], E. Tsitrone [b], the WEST team[1], the EUROfusion Tokamak Exploitation team[2]

[a] Aix Marseille Univ, CNRS, IUSTI, Marseille, France
[b] CEA, IRFM, F-13108 Saint-Paul-lez-Durance, France
[c] Department of Nuclear Engineering, University of Tennessee, Knoxville, TN 37996, USA
[d] Max-Planck-Institut für Plasmaphysik, 85748 Garching, Germany
[e] Aix Marseille Univ, CNRS, PIIM, Marseille, France,

A B S T R A C T

This paper summarizes the observations on the Unidentified Flying Object (UFO) observed during the first high fluence campaign performed in WEST. The campaign was characterized by high erosion and deposition rates, generating dusts and deposits prone to flaking during plasma operation. A total of 686 UFOs have been detected for 384 discharges executed, in which 133 UFOs lead to a disruption. These UFOs appear mostly during the low hybrid heating ramp-up early in the discharges. The mechanisms leading to a disruption is described as well as the delay available to react after the UFO entering in the plasma. The UFOs originate mostly from the high field side corresponding to the thick deposit area. These UFOs can be debris from a preceding disruption (≈27 %) or come from progressive loss of adherence of the thick deposits (≈55 %) under plasma cycling or more likely by disruption on this area. Finally, the thermal resistance of the poorly attached deposits has been calculated in the range from $2.10^{-4}$ °C $m^2$/W to $1.10^{-3}$ °C $m^2$/W coherent with previous observations in the high field side of the JET divertor.

## 1. Introduction

The Plasma-Facing Components (PFC) of next-step fusion devices will handle unprecedented heat fluxes and particle fluences. In particular, the first divertor of ITER is expected to operate until the end of the first DT campaigns, which corresponds to more than 2000 h of plasma discharge [1]. The WEST tokamak, equipped with an actively cooled tungsten ITER-grade divertor, is intended to evaluate the performance of the divertor under real tokamak conditions prior to ITER operation. A first high particle fluence campaign has been performed in WEST in 2023, resulting in about 3 h cumulated plasma duration with attached plasma condition in the lower divertor ($T_e \approx 25$ eV) [2]. The main limitation of this campaign was the appearance of Unidentified Flying Object (UFO) gradually hampering the discharge rate due to early disruption in the discharges.

This paper presents the UFO database built in WEST with bolometer and IR thermography systems. Sections 2 presents a summary of this high fluence campaign and description of the diagnostic set-up. Section 3 presents the UFOs characterization with their occurrence, timing and the classification of the UFOs depending on their impact on the discharges. Finally, the last section describes the IR analysis of these UFOs with their localization in the machine, the cause of their appearance and also their thermal characterization in terms of temperature and thermal resistance.

## 2. WEST high fluence campaign description

WEST is a superconducting tokamak with actively cooled PFC targeted at testing ITER tungsten divertor in a tokamak environment [3]. The WEST divertor consists of 12 independent toroidal sectors of 30°

* Corresponding author.
*E-mail address:* jonathan.gaspar@univ-amu.fr (J. Gaspar).
[1] : See http://west.cea.fr/WESTteam.
[2] : See the author list of "Overview of the EUROfusion Tokamak Exploitation programme in support of ITER and DEMO" by E. Joffrin Nuclear Fusion 2024.

https://doi.org/10.1016/j.nme.2024.101745
Received 13 June 2024; Received in revised form 27 August 2024; Accepted 20 September 2024
Available online 21 September 2024

each composed of 38 actively cooled ITER-grade PFCs for a total of 456 ITER-grade PFCs. The ITER-grade PFCs of WEST are based on the ITER divertor technology, with actively cooled tungsten monoblocks (MB) assembled on a copper heat sink in the radial direction [4]. The MBs have the 0.5 mm height toroidal bevel, 1° inclination of the top surface, as foreseen in ITER [5] to protect the leading edge from the almost perpendicular heat flux. On WEST, the lower divertor is flat and installed on the floor with 15° inclination below the magnetic X-point, with the two strike points impacting the same PFC. Therefore, the MB shaping has different orientation along the PFC in the inner strike point (ISP) region (MB #1 to #19) and outer strike point (OSP) region (MB #24 to #35). A transition area (MB #20 to #23) without shaping, to accommodate the private flux area, complete the PFC. The WEST lower divertor is monitored by a set of complementary thermal diagnostics allowing temperature measurements and heat load characterization [6]: 20 embedded thermocouples (TC) and 5 Fiber Bragg Grating (FBG) located at 5 mm below the top surface of the MBs and 13 InfraRed (IR) views [7]. The diagnostics are spread over the 12 divertor sectors keeping symmetric toroidal location of the sensors regarding the magnetic field toroidal modulation (ripple effect with 20° period). The diagnostics set-up and a simulated heat load pattern on the lower divertor showing the ripple effect are shown in the Fig. 1a).

In 2023, a first high particle fluence campaign has been performed from March 14th to April 12th 2023 [2], aiming at cumulating ITER relevant particle fluence on the divertor. The plasma scenario developed to optimize the divertor particle fluence is an attached L-mode plasma (Te≈25 eV) with Ip = 400 kA, $P_{LH}$=3.8 MW (lower hybrid heating), $n_e$ = 3.7 $10^{19}$ $m^{-2}$ (core plasma density) and pulse length ≈ 60–70 s, see Fig. 2b). 384 repetitive discharges were successfully performed, accumulating ≈3 h of plasma and ≈30 GJ of energy coupled to the plasma mainly by Low-Hybrid (LH) heating. A total fluence of 5.$10^{26}$ D/$m^2$ was reached at the OSP as measured with the flush Langmuir Probes (LPs), which corresponds to the range foreseen for ≈2 shots in the pre-fusion plasma operation phase of ITER [1]. The main limitation of the campaign was the appearance of UFOs entering in the core plasma and leading to MHD activity and disruption. These UFOs induce an impurity ingress with an increase of the radiated power and subsequent cooling of the core plasma. An example of a discharge with multiple small UFOs as observed at the end of the high fluence campaign is shown in Fig. 1b) with UFO events encircled.

## 3. The UFOs characterization

During the campaign, no operational cure has been found to avoid UFO production mainly due to the random behavior of the UFOs as function of time and space. To overcome this issue, an UFO database has been made to classify the UFOs, determine the number of occurrences, their timing, and their impact on the plasma discharge.

### 3.1. UFO classification and production

These UFOs are classified into three classes according to how they affect the discharge by looking at the variation of the radiated power ($P_{RAD}$), the line integrated plasma density ($n_e$), the plasma current ($I_p$), the injected power with the Low Hybrid Heating system ($P_{LH}$), the central electron temperature ($T_e(0)$) and the plasma energy content ($W_{MHD}$), Fig. 2 shows the evolution of these quantities for the three different classes. The first class consists of small impact UFOs (class 1), for which the plasma will survive and return back to its original state. The impurity ingress cools the core plasma temporally, but the plasma is resilient and the discharges continue with only a reduction of the pulse duration due to the transient increase of loop voltage ($V_{loop}$) during the UFO event. The second group consists of medium-impact UFOs (class 2) with important core plasma cooling (below 2 keV) due to the larger impurity ingress in the core plasma, resulting to a bifurcation in a"cold branch" regime [8] prone to magneto-hydrodynamic (MHD) instabilities systematically followed by a disruption up to several seconds later. The third group consists of major impact UFOs (class 3) leading to radiative collapse of the plasma and fast disruption typically within 200 ms.

The 384 discharges successfully executed have been manually analyzed to determine the occurrence of each class. Only UFO leading to a $P_{RAD}$ increase ≥ 200 kW (10 % of the total radiated power), while $P_{LH}$ is constant, have been kept. A total of 686 UFOs has been found with 553 class 1, 116 class 2 and 17 class 3. This indicates that a total of 133 discharges (≈35 %) ended by a disruption due to an UFO among the

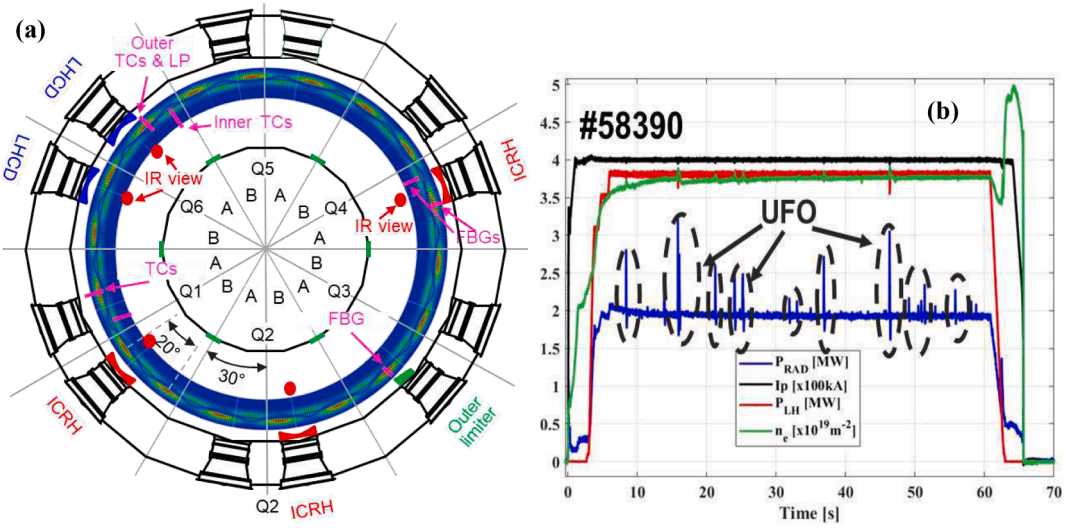


**Fig. 1.**

**(a)** Top view of the machine with typical heat load pattern on the lower divertor due to the ripple modulation (20°), the sector distribution, the antennas and the heat load diagnostics and infrared views. **(b)** Pulse #58390, time evolution of **plasma current (Ip [x100kA])**, **line integrated central density ($n_e$ [x$10^{19}$$m^{-2}$])**, **Low Hybrid power ($P_{LH}$ [MW])**, and **total radiated power ($P_{rad}$ [MW])** with UFO events encircled.

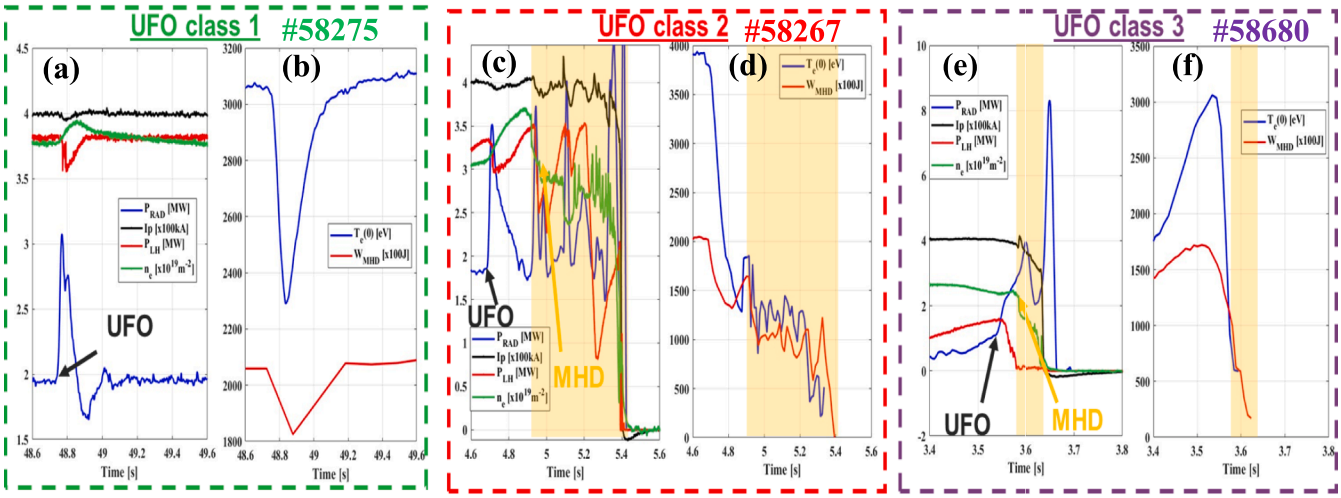


**Fig. 2.**

Impact on the discharges for the three UFO classes: **(a), (c) and (e)** time evolution of **plasma current (Ip [x100kA])**, **line integrated central density ($n_e$ [x$10^{19}$m$^{-2}$])**, **Low Hybrid power ($P_{LH}$ [MW])**, and **total radiated power ($P_{rad}$ [MW]). (b), (d) and (f)** time evolution of **central electron temperature ($T_e(0)$ [keV])** and **plasma energy content ($W_{MHD}$ [x100J])**. MHD activity in the cold branch overlay **in orange**.

total number of disruptions of 250 (disruptivity rate of 65 %). Fig. 3a) shows the evolution of the cumulated number of UFOs for each class versus the cumulated plasma duration and corresponding maximal D fluence computed with the flush Langmuir Probes (LPs). The first UFO of each class appears after a cumulated duration of 66 s, 1069 s and 4311 s for the UFO class 1, 2 and 3, respectively. The fast apparition of the UFO class 1 is due to dust and layers accumulated on the divertor [9] from the previous plasma experiments performed before the start of the high fluence campaign, from January 10th to March 14th, with a cumulated plasma duration of ≈2h25 min and ≈13 GJ of energy coupled to the plasma with wide variety of injected power and magnetic equilibriums. Fig. 3b) shows the number of UFO per minute for each class and the total. These numbers increase during the campaign up to a relative constant value around 6 UFO/min, for the total of all classes, but more importantly the class 2 (leading to disruption) seems stationary after ≈2h of plasma to a value around 1.5 UFO/min. Considering the duration of the discharge of 1 min this shows the high impact of the UFO on the plasma operation (considering also that sometimes few pulses are required to recover from the disruption). For the whole high fluence campaign, 250 discharges among 384 exhibits at least one UFO (65 %) with a maximum of 12 class 1 UFO in a single discharge and only 19 discharges (5 %) longer than 50 s are UFO free.

### 3.2. *UFO timing & impact on plasma discharges*

Fig. 4a) shows the histogram of the time when the UFOs entering in the plasma for the three UFO classes, the vertical dashed lines are the $P_{LH}$ ramp-up phase between 3 and 6 s. For the class 1, 180 UFOs (33 %) among 553 occur during the LH ramp-up then are uniformly distributed throughout the discharges duration. For the classes 2 and 3, 80 UFOs (60 %) among 133 are in the LH-ramp-up phase. Few class 1 (4 %) and class 2 UFOs (7 %) are detected before the LH phase, around 2 s, when the magnetic equilibrium goes from limiter (on the main chamber inboard limiters) to the X-point configuration. Fig. 4b) illustrates the delay between the UFO appearance and the plasma end (whether it is from a disruption or from the programmed waveforms), this gives the time available to react after the entering of the UFO in the plasma. The delay for the class 1 is quite uniformly distributed over the typical

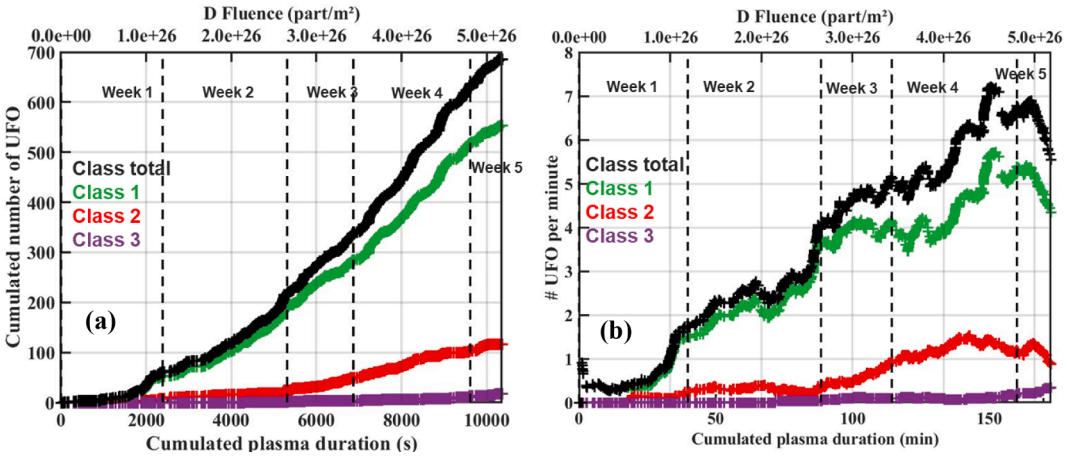


**Fig. 3. (a)** Cumulated number of UFOs and **(b)** number of UFOs per min as function of the cumulated plasma duration and peak D fluence for the different classes and the total.

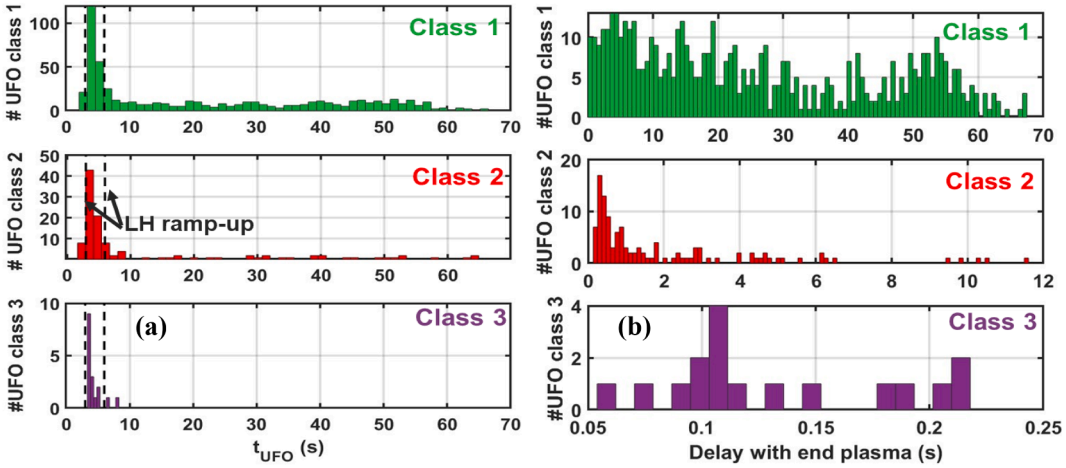


**Fig. 4.** Histogram of **(a)** UFO appearance time ($t_{UFO}$) and **(b)** delay with the plasma end (Ip = 0kA) for the different UFO classes (553 class 1, 116 class 2 and 17 class 3).

discharge duration of 1 min as expected. The delay for the class 2 is shorter as this kind of UFO induces the disruption, the median is about 1 s and 35 % are between 200 ms and 500 ms. Finally, the delay for the UFO class 3 is about 100 ms and the fastest is 54 ms. This is higher than the disruption triggered by UFO on other machine as C-mod where disruption in 2 ms has been observed with Molybdenum UFO [10].

Fig. 5 shows the impact of the UFOs on the radiated power, the central electron temperature and the plasma energy content for the different classes. The UFOs class 1 induce a moderate increase of $P_{RAD}$ lower than 1 MW (50 % of $P_{RAD}$ before UFO), leading to a small reduction of the plasma energy (about 5 %) and more importantly a core temperature still in the range of 3 keV. For the classes 2 and 3 the $P_{RAD}$ increase is higher resulting to plasma energy decrease from 20 % to 60 % and a core temperature in the range of 1 keV. This plasma cooling leads to a bifurcation into the "cold branch" regime with low central temperature and degraded LH absorption preventing the central heating of the plasma and MHD instabilities leading to the disruption [8]. To avoid the disruption with UFO class 2, an additional central electron heating would be necessary to increase the central temperature above 3 keV in the stable domain of the tungsten cooling factor. A first evaluation of the UFO composition has been done using bolometry inversion and Bremsstrahlung emission for the effective ion charge $Z_{eff}$. It is shown that most of the UFOs are mainly composed of tungsten to match the bolometry line of sights and the $Z_{eff}$ variation. The tungsten mass mobilized in the UFO has been evaluated in the range of 14 μg, 64 μg for class 1 and 2 respectively. Only few events of class 3 were evaluated, with an average of 110 μg.

## 4. IR analysis

The WEST IR system is composed of 13 IR views with 6 divertors views (covering 85 % of the divertor), 5 antennas views (100 % of the antennas), one wide angle view and one high resolution view. Fig. 6 a) shows an example of one part of an IR divertor view. Thanks to this wide coverage and the UFO detection performed in the previous section, the IR movies have been analyzed to detect the UFO trajectories and determine their location before their take-off and entering in the plasma (see Fig. 6 b) to g)). For the classes 2 and 3, 111 UFOs (83 %) among 133 have been detected which is coherent with the divertor coverage by the IR system of 85 %. For the class 1, 339 UFOs (61 %) among 553 have been detected, this lower value is explained by the fact that small UFOs ($\Delta P_{RAD}$<400 kW) are difficult to detect due to their small size and short lifetime before full ablation. Nevertheless, a large number of UFOs were detected, making it possible to carry out a statistical study of the various quantities, such as their location (sector, PFC number and MB) and their thermal behavior before their detachment (temperature, thermal

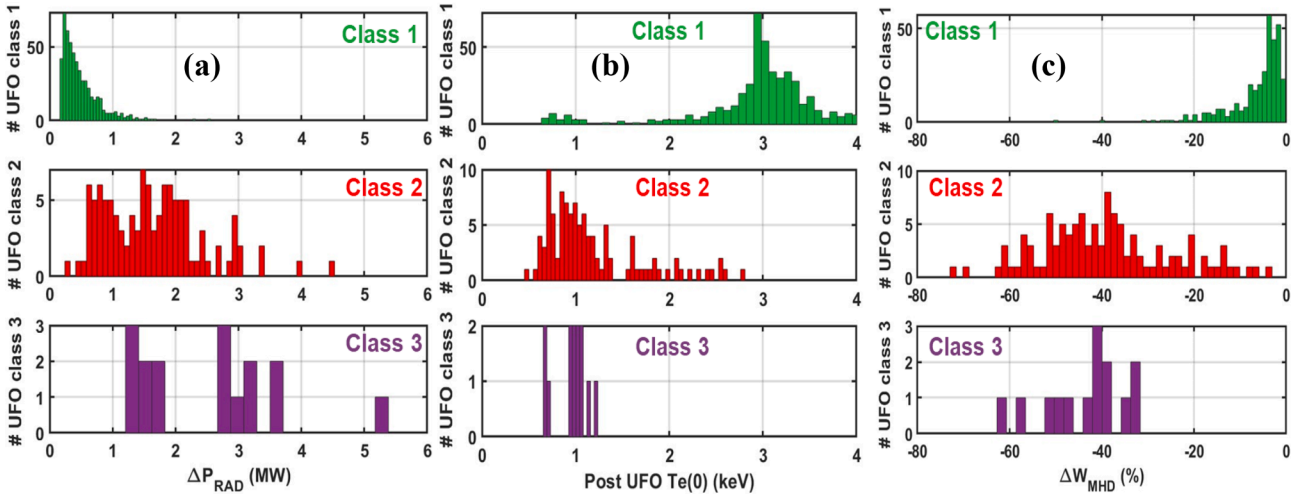


**Fig. 5.** Histogram of UFO impact on **(a)** total radiated power increase ($\Delta P_{RAD}$) **(b)** central electron temperature ($T_e(0)$) and **(c)** plasma energy content ($W_{MHD}$) for the different UFO classes.

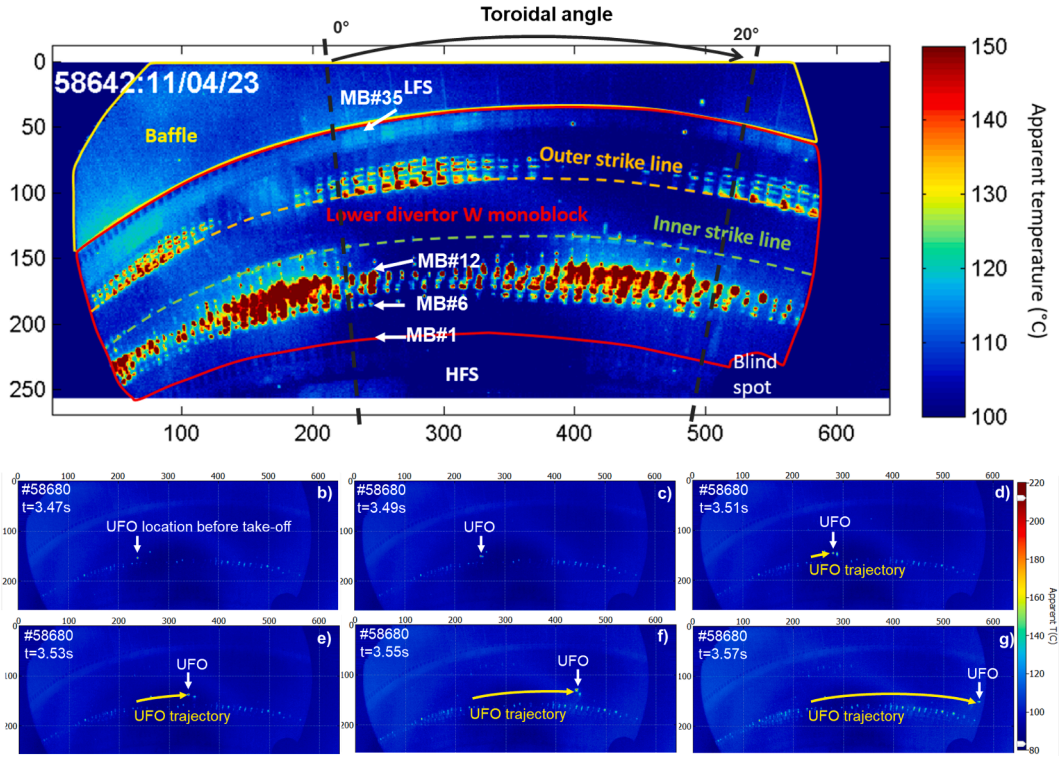


**Fig. 6.** **(a)** Example of IR divertor view of the lower divertor during the last week of the high fluence campaign. **(b)** to **(g)** example of UFO trajectory with UFO location before take-off.

resistance). Note that the apparent size and temperature of UFOs on IR images (which can change during the trajectory) are linked to their actual size and temperature, although the two criteria cannot be dissociated (a small, hot UFO has the same trace as a larger and colder one).

### 4.1. UFOs location

Fig. 7a) shows the histogram of the UFOs sector location for the three classes with indication of the sectors with poor IR coverage. The lower divertor in WEST is composed by 12 divertor sectors, each having 30° toroidal extension which is also equivalent to 1.5 magnetic field toroidal modulation period in WEST (20°). The sectors located in module A (QXA) exhibit higher UFO production about twice higher than the module B sectors (QXB). This is explained by the Fig. 7b) showing the histogram of the UFO versus the toroidal angle mapped on a ripple period (20°) as important toroidal modulation of the magnetic line (called ripple effect) is present in WEST. The UFO production occurs mainly in the maximum inner heat load area. Module A sector (QXA) exhibits two maximum inner heat load areas and module B sector (QXB) only one, this explains the previous statement. Considering that the UFO production appears uniform at the machine scale for all ripple period in all sectors.

At the PFC scale in the radial direction, the Fig. 8a) shows that the UFO production occurs mainly on the High Field Side (HFS) for all

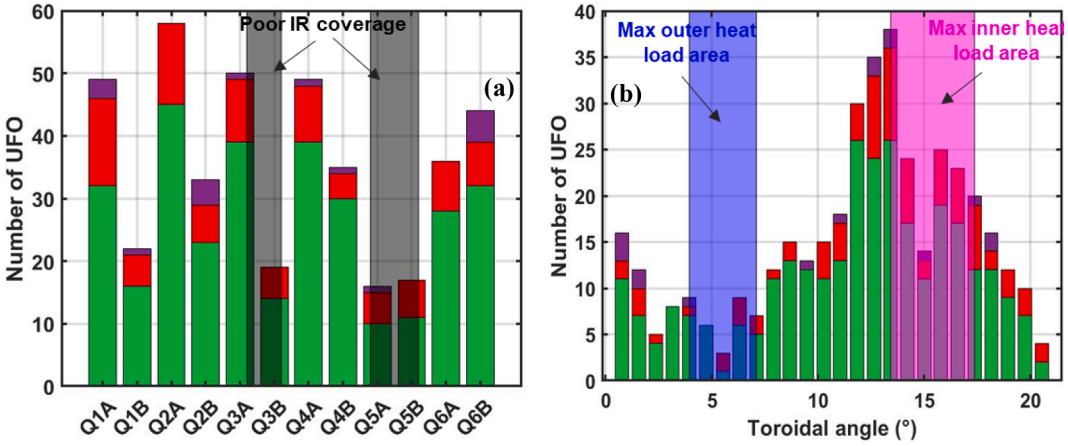


**Fig. 7.**

Histogram of UFO (class 1/ class 2/ class 3) location versus **(a)** sectors and **(b)** toroidal angle mapped on a ripple period (20°) with overlay for the maximal heat load areas for the **outer** and **inner** sides.

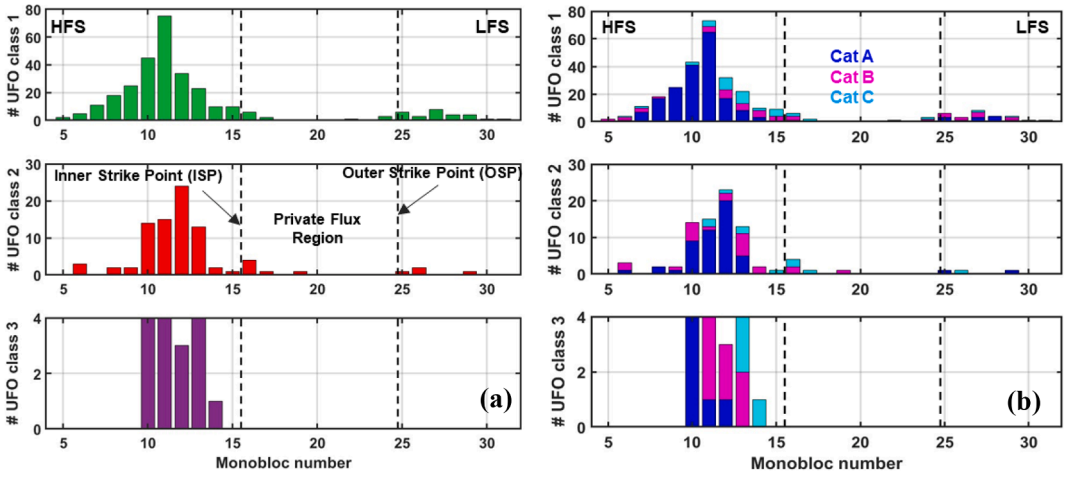


**Fig. 8.**

Histogram of UFO versus monobloc number **(a)** for class 1/ class 2/ class 3 and **(b)** for category A/ category B / category C with outer and inner strike point location (vertical dashed lines).

classes from MB number 8 to 12 corresponding to the thick deposit area [11], few MBs away from the ISP position, in the far scrape off layer (SOL). Post-mortem observations of this area show that, during the high fluence campaign the thick deposit is mainly composed by a tungsten dense layer [12] coherent with UFOs mainly composed of tungsten. A small number of UFOs originate from the Low Field Side (LFS) where thin foil deposits have been observed in the shadowed area [2] and from the private flux region without deposit on the MB. To determine the origin of the UFOs, the previous pulses have been analyzed to understand the mechanisms of the UFO birth. Three different UFO birth categories have been defined. The category A is an UFO detaching from a thick deposit area with poor thermal contact. In this case, during the previous pulses the UFO area exhibits high temperature with fast variation following the time evolution of the injected power as illustrate in the Fig. 9a) with a detailed discussion. The UFO category B is a debris produced by a disruption during the previous discharge or few discharges before. In this case we can observe that during a previous pulse, mainly the last one, a disruption occurs creating a lot of debris with one debris ending up in the area identified as the UFO (same pixels) at the following discharge. The UFO category C is an "undetermined" population as, during the previous discharge, the UFO were "cold" without indication of poor thermal contact and no debris has been observed during the previous disruption (even if the determination of the debris can be difficult with low temperature contrast). Fig. 8b) shows the histogram of UFOs versus the MB number for the different categories of causes. For the classes 2 and 3 about 30 UFOs (27 %) are debris (category B in magenta) from preceding disruptions. For the class 1, 459 UFOs (83 %) are coming from thick deposit (Cat. 1 dark blue) and 58 UFOs (17 %) from debris (Cat. B magenta). The debris are mainly on the HFS as they originate from the thick deposit area when disruption occurs in this area. Fig. 8b) shows also that UFOs originating from the LFS and the private flux region are mainly debris from preceding disruptions (Cat. B in magenta). In addition, 9 category B UFOs originate from the baffle. At this point no precursor has been found as for every disruption a large plume of hot debris of the PFCs can be observed in the IR movies but a very few numbers of these debris become an UFOs in the next discharges.

The category A (dark blue) is the main cause of the UFO production

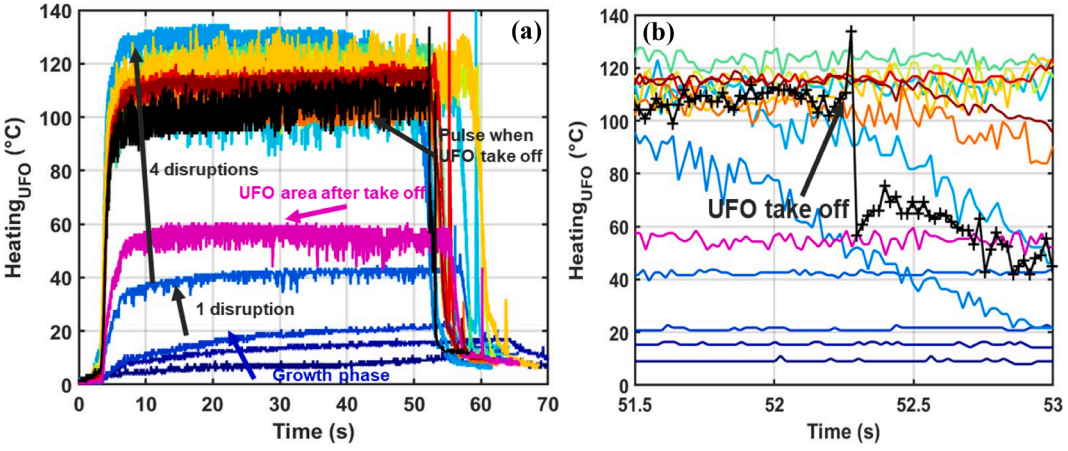


**Fig. 9.**

Time evolution of the surface temperature at class 2 UFO of the pulse #58583 from the beginning of the high fluence campaign to the UFO appearance (color gradation from **blue** to **red**), pulse with UFO appearance #58583 at $t_{UFO}$=52.3s (**black**) and next pulse (**magenta**). **(a)** full discharges **(b)** zoom in at the $t_{UFO}$=52.3s.

for all classes, with 204 UFOs (60 %) for the class 1 and 61 UFOs (55 %) for the classes 2 and 3. It is therefore necessary to study the cycling of these poorly attached deposits to understand the reason of this poor thermal contact and analyze if precursor of UFO can be defined. Several category A UFOs have been analyzed and the disruption seems also to play an important role in this category of UFO. Fig. 9a) shows the heating evolution of the surface layer during the campaign with color gradation from the start (dark blue #58174) to the UFO take-off (black #58583) and the heating after the UFO for the remaining deposit (magenta #58595). At this location the heating of a MB without surface deposit is in the range of 10 °C as for the first curve for the discharge #58174. The third curve with heating up to 20 °C corresponds to the discharge #58308 after 3740 s of cumulated plasma duration. This heating increase can be attributed to the growth phase of the surface deposit, with increasing thickness and thermal resistance. Then a fast increase of the heating is observed from 20 °C to 40 °C for the discharge #58318 only 54 s of plasma exposure after the discharge #58308 but with a disruption on the lower divertor. After this discharge, 4 disruptions occur and for the discharge #58323 an important heating in the range of 120 °C is observed. Finally, the heating remains almost constant in the range of 100–120 °C during 5230 s of cumulated plasma, hundreds of cycling and many disruptions, then during the discharge #58583 a part of the surface deposit detached at 52.3 s in the discharge and leads to a disruption (black curve). Fig. 9b) illustrates that no precursor on the thermal behavior indicates the imminent UFO event. After this, the heating of this area remains in the range of 60 °C (magenta curve) showing that a part of the deposit remains on the component with poor thermal contact, but no further evolution has been observed. The heating history of more UFO must be analyzed to confirm the impact of the disruption in the degradation of the thermal contact.

### 4.2. Thermal analysis of the surface layer

Fig. 10a) shows the histogram of the surface temperature of the UFO areas just before the UFOs. The surface temperature is obtained from the blackbody temperature measured by the IR system and converted in real temperature considering an emissivity of 0.8 which is the range measurement in these areas [13] and blackbody surrounding temperature of 70 °C which is the temperature of the water in the cooling pipes. At this stage no correction of the spatial resolution has been done [14] leading to a potential under-estimation of the real temperature of the deposit. The temperature range is mainly from 100 to 300 °C corresponding to heating from 30 to 230 °C and depends on the location of the deposit (MB number) and the surface heat flux varying from 2.2 MW/m$^2$ close to ISP (MB#15) down to 0.25 to 0.1 MW/m$^2$ in the thick deposit area from MB#12 to MB#7, respectively. The heat flux distribution has been estimated from the FBG measurements [15]. With the knowledge of the surface temperature of the deposit at the steady state and the temperature of water circulating in the MB, the thermal resistance of surface deposit can be calculated. Fig. 10b) shows the histogram of the UFO versus their thermal resistance in log scale. The thermal resistance of these areas is in the range from $2.10^{-4}$ to $1.10^{-3}$ °C m$^2$/W. These values are in the range of previous observations in JET with carbon wall with thermal resistance of carbon deposit from 6.2 $10^{-5}$ to 1.5 $10^{-3}$ °C m$^2$/W [16] and also in the JET ITER-like wall with thermal resistance of Beryllium of $5.10^{-4}$ °C m$^2$/W [17].

## 5. Conclusion

The first deuterium high fluence campaign performed in WEST cumulates ≈3h of plasma in L-mode attached divertor condition and a maximum fluence of ≈$5.10^{26}$ part/m$^2$ with 384 discharges executed. One of the main outcomes of the campaign is the progressive appearance of UFOs, significantly hampering operation after ~2 weeks of repetitive pulses. An UFO database has been built with a total of 686 UFOs detected and classified into three classes depending on their impact on the plasma discharge. A total of 133 UFOs leading to a disruption (classes 2 and 3) have been identified (a third of the executed pulse number). The frequency of the UFOs increased over the weeks up to a relative stationary value of ≈6 UFO/min for all classes and ≈1.5 UFO/min for UFOs leading to a disruption. At the end of the campaign, most of the pulses were affected by UFO leading to disruption. The UFOs appear mainly during the early phase of the discharge, during the heating power ramp-up (≈60 %). The disruptions induced by the UFOs (classes 2 and 3) are due to the core plasma cooling from $T_e(0)$ 3–4 keV down to 1 keV leading to a radiative collapse followed by a disruption. For these UFOs the delay between the UFO appearance and the disruption is mainly in the range from 100 ms to 1 s with delay up to 12 s and fastest disruption in 54 ms.

The wide IR coverage allowed the localization of most of the UFOs. They originate predominately from the HFS in the maximum inner heat load areas where thick deposits are observed. The main cause of the UFO production appears to be the disruptions on the lower divertor by different ways. For the UFOs leading to a disruption, ≈27 % of the UFOs are debris from a preceding disruption and ≈55 % are due to cycling of deposit with poor thermal contact that seems initiated by disruption on

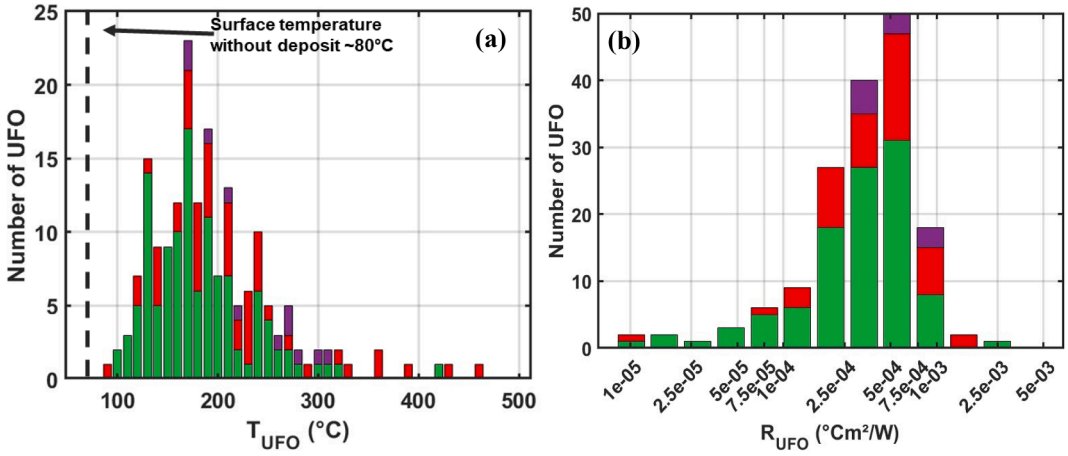


**Fig. 10.**

Histogram of UFO (**class 1**/ **class 2**/ **class 3**) **(a)** surface temperature ($T_{UFO}$) and **(b)** UFO thermal resistance ($R_{UFO}$).

the thick deposit area. Finally, the thermal resistance of the poorly attached deposit has been calculated in the range from $2.10^{-4}$ to $1.10^{-3}$ °C.m$^2$/W coherent with previous observation in the HFS of the JET divertor. A cleaning of the divertor has been performed using an adhesive technique during the shut-down after the high fluence campaign before the following campaign started in winter 2023. More advanced techniques are under development to improve the cleaning of the divertor during future shutdown. In parallel, cooling of the divertor using impurity seeding are under development to cool the plasma edge and reduce the erosion and material deposition to increase the fluence capabilities in WEST.

## CRediT authorship contribution statement

**J. Gaspar:** Writing – review & editing, Writing – original draft, Visualization, Validation, Software, Methodology, Investigation, Formal analysis, Data curation, Conceptualization. **Y. Anquetin:** Writing – review & editing, Investigation, Data curation. **Y. Corre:** Writing – review & editing, Resources, Methodology, Formal analysis, Conceptualization. **X. Courtois:** Resources, Investigation, Data curation. **M. Diez:** Investigation, Formal analysis, Data curation. **A. Ekedahl:** Validation, Resources, Project administration, Funding acquisition. **N. Fedorczak:** Visualization, Resources, Methodology, Investigation, Conceptualization. **A. Gallo:** Writing – review & editing, Investigation, Formal analysis, Conceptualization. **J-L. Gardarein:** Supervision, Resources, Project administration, Formal analysis. **J. Gerardin:** Supervision, Resources, Project administration, Formal analysis. **J. Gunn:** Investigation, Data curation, Conceptualization. **A. Grosjean:** Formal analysis, Data curation. **K. Krieger:** Validation, Supervision, Resources, Project administration, Conceptualization. **T. Loarer:** Investigation, Formal analysis. **P. Manas:** Writing – review & editing, Validation, Methodology, Investigation, Data curation, Conceptualization. **C. Martin:** Writing – review & editing, Methodology, Investigation. **P. Maget:** Writing – review & editing, Validation, Methodology, Formal analysis, Conceptualization. **R. Mitteau:** Methodology, Formal analysis. **P. Moreau:** Validation, Software, Methodology, Formal analysis, Data curation, Conceptualization. **F. Rigollet:** Writing – review & editing, Visualization, Validation, Methodology, Conceptualization. **E. Tsitrone:** Writing – review & editing, Validation, Resources, Project administration, Investigation, Funding acquisition, Formal analysis, Conceptualization.

## Declaration of competing interest

The authors declare that they have no known competing financial interests or personal relationships that could have appeared to influence the work reported in this paper.

## Data availability

Data will be made available on request.

## Acknowledgments

This work has been carried out within the framework of the EUROfusion Consortium, funded by the European Union via the Euratom Research and Training Programme (Grant Agreement No 101052200 — EUROfusion). Views and opinions expressed are however those of the author(s) only and do not necessarily reflect those of the European Union or the European Commission. Neither the European Union nor the European Commission can be held responsible for them.

## References

[1] R.A. Pitts, et al., Physics basis for the first ITER tungsten divertor, Nucl. Mater. Energy 20 (100696) (2019), https://doi.org/10.1016/j.nme.2019.100696.
[2] E. Tsitrone et al., "Overview of plasma wall interactions in the first high particle fluence campaign of WEST" this conference.
[3] J. Bucalossi, et al., Operating a full tungsten actively cooled tokamak: overview of WEST first phase of operation, Nuclear Fusion 62 (2022) 042007, https://doi.org/10.1088/1741-4326/ac2525.
[4] M. Missirlian, et al., Manufacturing, testing and installation of the full tungsten actively cooled ITER-like divertor in the WEST tokamak, Fusion Eng. Design 193 (2023) 113683, https://doi.org/10.1016/j.fusengdes.2023.113683.
[5] R.A. Pitts, et al., Physics conclusions in support of ITER W divertor monoblock shaping, Nucl. Mater. Energy 12 (2017) 60–74, https://doi.org/10.1016/j.nme.2017.03.005.
[6] J. Gaspar, et al., Divertor power loads and scrape off layer width in the large aspect ratio full tungsten tokamak WEST, Nuclear Fusion 61 (2021) 096027, https://doi.org/10.1088/1741-4326/ac1803.
[7] X. Courtois, et al., Full coverage infrared thermography diagnostic for WEST machine protection, Fusion Eng. Design 146 (2019) 2015–2020, https://doi.org/10.1016/j.fusengdes.2019.03.090.
[8] V. Ostuni, et al., Core radiative collapse characterisation and integrated modelling in WEST plasmas, Nucl. Fusion 62 (2022) 106034, https://doi.org/10.1088/1741-4326/ac8cd6.
[9] J. Gerardin et al., "Evolution and cleaning of the deposit layers on the lower divertor of WEST fully equipped with ITER grade components", this conference.
[10] R. Granetz et al., "Comparison of high-Z triggered disruptions in metal-walled tokamaks" 65th APS DPP conference.
[11] M. Diez, et al., Overview of plasma-tungsten surfaces interactions on the divertor test sector in WEST during the C3 and C4 campaigns, Nucl. Mater. Energy 34 (2023) 101399, https://doi.org/10.1016/j.nme.2023.101399.
[12] C. Martin et al., "Post-mortem analysis of the deposit layers on the lower divertor after the high particle fluence campaign of WEST", this conference.
[13] J. Gaspar et al., "Overview of the emissivity measurements performed in WEST: in-situ and post-mortem observations", Nuclear Fusion, accepted paper. 10.1088/1741-4326/ac6f68.
[14] Y. Corre, et al., Methodology for heat flux investigation on leading edges using infrared thermography, Nuclear Fusion 57 (2017), https://doi.org/10.1088/0029-5515/57/1/016009.
[15] Y. Anquetin et al., " Identification of a double decay length ($\lambda_q^t$) heat flux deposition shape with embedded thermal measurement and neural network", this conference.
[16] J. Gaspar, et al., In-situ estimation of the thermal resistance of carbon deposits in the JET tokamak, Int. J. Therm. Sci. 104 (2016) 292–303, https://doi.org/10.1016/j.ijthermalsci.2016.01.022.
[17] T. Wauters, et al., Isotope removal experiment in JET-ILW in view of T-removal after the 2nd DT campaign at JET, Physica Scripta 97 (2022) 044001, https://doi.org/10.1088/1402-4896/ac5856.